Low-Noise Optical Accelerometers: Bridging the Gaps among Geophones, Accelerometers, and Broadbands in a Deep Borehole

Chet Hopp*¹, Taka'aki Taira², Michelle Robertson¹, Joseph J. Farrugia³, Corinne Layland-Bachmann¹, and Ernie Majer¹

Abstract

Earthquakes and other seismic sources produce waves with frequency content spanning many orders of magnitude. Recording a broader frequency band of interest has historically required deploying multiple instruments designed to work the best within limited, overlapping frequency ranges. Here, we detail a 300 m deep borehole deployment of a sensor package, including three new optical accelerometers that can potentially replace many dedicated instruments with a single, low-noise sensor. These instruments are designed with a flat frequency response from 0.005 to 1500 Hz, spanning the flat response segments of broadband sensors and geophones, as well as a low-noise floor and high sensitivity. The sensors have been functioning normally for over four years, fully grouted at depths of > 100 m. Year-long power spectral density (PSD) profiles show that the optical accelerometers have a lower noise floor than a colocated geophone for all frequencies, with 20 dB noise reduction at 250 Hz. PSD comparisons to a broadband sensor installed at the surface show a 5-30 dB noise reduction for the optical accelerometer above 1 Hz, although this is likely due, in part, to the broadband sensor being subjected to much higher surface noise. At periods > 5 s, the broadband sensor shows up to 20 dB lower noise than the optical accelerometer, which in turn has up to 50 dB lower noise floor than the colocated geophone. Finally, modeling the Brune displacement spectrum for theoretical seismicity within 1 km of the borehole shows that the optical accelerometers could potentially deliver a detection threshold improvement of one magnitude unit relative to the colocated geophone.

Cite this article as Hopp, C., T. Taira, M. Robertson, J. J. Farrugia, C. Layland-Bachmann, and E. Majer (2022). Low-Noise Optical Accelerometers: Bridging the Gaps among Geophones, Accelerometers, and Broadbands in a Deep Borehole, *Seismol. Res. Lett.* **93**, 2367–2376, doi: 10.1785/0220210340.

Supplemental Material

Introduction

Observations of elastic waves in the Earth cover an immense range of frequencies from thousands of seconds period (e.g., normal modes; Benioff *et al.*, 1961) to hundreds of kilohertz (e.g., Plenkers *et al.*, 2010). Recording waves over such a broad frequency spectrum has typically required the deployment of many different dedicated sensors, including strain gauges, Global Navigation Satellite System receivers, broadband seismometers, geophones, force-balance accelerometers, piezoelectric accelerometers, piezoelectric "acoustic emission" sensors, and many more. If we limit the scope of observation to only unstable seismic slip (i.e., an earthquake), the band of potential frequencies still spans from mHz to hundreds of kilohertz, depending on source–receiver distance and the size of the fault or fracture that ruptured. To cover this range of frequencies, typically a broadband sensor would be used to record the range

of megahertz to tens of hertz and be paired with a colocated strong-motion accelerometer or geophone to record higher frequencies and avoid clipping at large ground motions. Recently, a new class of sensor has been developed that couples high sensitivity and low noise with the high corner frequencies and convenience of geophones. These so-called ultralow-noise accelerometers are sensitive across the combined frequency band of standard broadband instruments and geophones while maintaining a low-noise floor, particularly at frequencies >1 Hz.

^{1.} Lawrence Berkeley National Laboratory, Earth and Environmental Sciences Area, Berkeley, California, U.S.A., https://orcid.org/0000-0002-7980-0494 (CH);
2. Berkeley Seismology Lab, Berkeley, California, U.S.A., https://orcid.org/0000-0002-6170-797X (TT);
3. Pacific Geoscience Centre, Geological Survey of Canada, Sidney, British Columbia, Canada, https://orcid.org/0000-0002-4607-3104 (JJF)

^{*}Corresponding author: ChetHoppchopp@lbl.gov

[©] Seismological Society of America

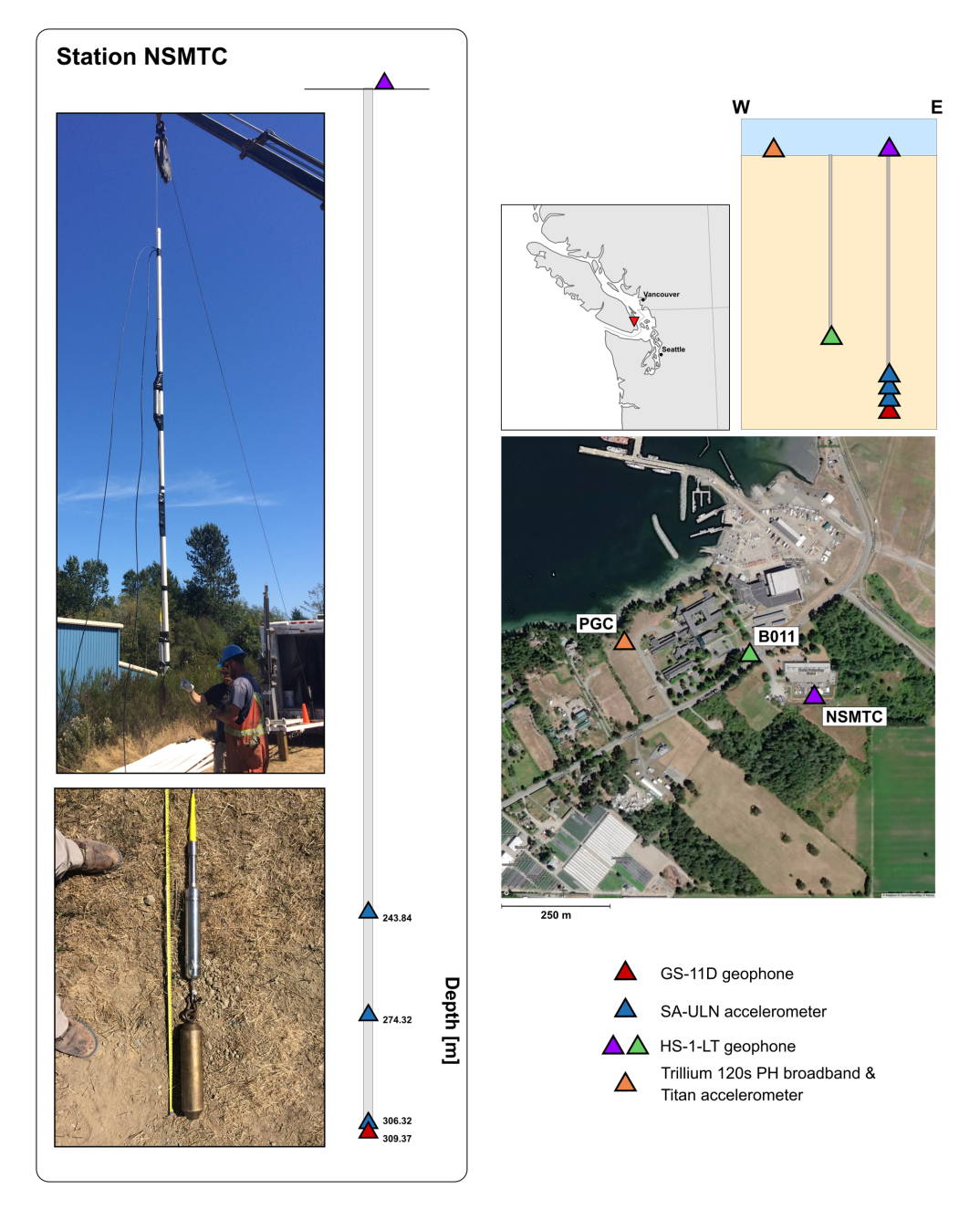


Figure 1. Overview of the North Saanich Marine Technology Center (NSMTC) borehole site. On the left is a scale schematic of the sensor locations in the borehole accompanied by photos of the installation and the bottom-hole geophone sonde before install. To the right, we show the location of the field site including the wellhead for NSMTC (purple) and the locations of the other sensors used for comparison purposes in this article. In orange is station CN.PGC, and in green is the wellhead location of PBO station PB.B011. A cartoon cross section illustrates the spatial relationships between the sensors. The color version of this figure is available only in the electronic edition.

Here, we describe a deep borehole installation of three Silicon Audio Ultra-Low Noise (SA-ULN) accelerometers in Sidney, British Columbia, Canada, and compare these publicly available data to colocated geophones and nearby broadband sensors to assess their utility as a "one size fits all" seismic monitoring solution.

Instrument Deployment SA-ULN

The SA-ULN accelerometer sensing element is an optical interferometer used to interrogate the displacement of the sensing mass. The sensing mass is held in place by springs, but a magnetic actuator provides the restoring force. This design is akin to a standard force-balance strong motion accelerometer, but the displacement of the mass is precisely measured by optical interferometer, instead of the displacement of the mass producing a current that can be related to the acceleration of the sensor, allowing the force feedback to create a much larger dynamic range and a lower noise floor than standard instruments, while maintaining sensitivity across broad frequency band (Table 1; Marusiak et al., 2021). The sensors are available in a "high-sensitivity" and a "high-dynamic range" configuration among other options (Table 1). The configuration used in this study is the "high-sensitivity" version with a sensitivity of 60 V/g, a fullscale output of ±0.5g, and a dynamic range of 172 dB. SA-ULNs are available in a number of form factors (posthole, vault, single component), but they were packaged into a pressuretested sonde by ASIR Seismic for installation in a deep borehole (Fig. 1).

Cascadia borehole site

The site selected for the bore-

hole observatory detailed in this study is the North Saanich Marine Technology Centre (NSMTC) on Vancouver Island in Sidney, British Columbia, Canada (Fig. 1). The six-inch, uncased borehole was drilled in granite to 311 m below ground level(~1021 ft) in early August 2017. On 17 August, an array of three SA-ULN optical accelerometers and a single, three-

TABLE 1
Sensor Specification Comparison for a Selection of Commercially Available Accelerometers, Broadbands, and Geophones

Instrument	Sensitivity (V/g)	Full-Scale Output (<i>g</i>)	Full-Scale Output (Vpp)	Dynamic Range (dB @ 1 Hz)	Frequency Response (Hz)	Power (W)
SA-ULN (high-dynamic range)	15	±2	60	183	0.004–800	0.15
SA-ULN (high-sensitivity version)	60	±0.5	60	172	0.005–1500	0.15
Nanometrics Titan	5, 10, 20, 40, 80	±4, 2, 1, 0.5, 0.25	40	166	DC-430	1.1
Guralp Fortis	2.5, 5, 10, 20	$\pm = 4, 2, 1, 0.5$	40	>160	DC-100	1.5
Kinemetrics Episensor ES-T	Selectable (gain and output)	±4, 2, 1, 0.5, 0.25	5, 20 se; 10, 40 diff	155	DC-200	0.29–0.84
Geotech PA-23	2.5	±4, 2, 1, 0.5	40	142	DC-100	<1.5
Nanometrics Trillium Compact Horizon	750 V/ms ⁻¹		40	>152 dB	0.0083–180	0.18
Guralp3 T-120	1500 V/ms ⁻¹		40	>167 dB	0.0083–50	0.75
Geospace HS-1	18.11 V/ms ⁻¹			>124 dB	1–500	n/a
Geospace GS-11D	32 V/ms ⁻¹					

diff, differential; SA-ULN, Silicon Audio Ultra-Low Noise; se, single-end.

Many of the sensors are available in various configurations, so we have listed the selectable gain and output options. The SA-ULN is available in a "high-dynamic range" and "high-sensitivity" version, although the version of the instrument installed in the field site detailed in this article was the $\pm 60 \text{ V/g}$ "high-sensitivity" version. Direct comparisons are not as straightforward for broadbands and geophones, so we have reported the "standard" package for these instruments.

component Geospace GS-11D geophone was lowered into the well on wireline to near total depth. A weight was attached to the geophone to anchor the array against buoyant movement during grouting (Fig. 1). The weighted geophone was installed at a depth of 307.8 m, with the SA-ULN sondes installed at depths of 304.8, 274.3, and 243.8 m (Table 2). In addition, a single loop of single-mode fiber optic cable was installed to a depth of 306.3 m. The entire depth of the borehole was grouted in three stages that occurred on 18, 22, and 27 August 2017. The first stage of grouting (18 August 2017) filled the lower 225 m of borehole, enough to cover the shallowest SA-ULN sensor to a depth of 158 m. A single Geospace HS-1-LT three-component geophone was installed~10 m from the wellhead, buried ~0.5 m into the levee that was used as a drill pad. On 19 August, data recording began using Reftek 130 digitizers located in a control hut near the top of the borehole and were sampled at 500 Hz.

The nearby Ocean Networks Canada (ONC) headquarters provides the infrastructure for data telemetry from the borehole. The SEED network and station id for the borehole site is NV.NSMTC (Neptune network; Ocean Networks Canada, 2009). The four borehole sensors and one surface geophone are distinguished by their location code. Table 2 summarizes the types of sensors and their positions in the borehole with location codes G1 and G2 representing the surface geophone and the downhole geophone, respectively. The SA-ULN

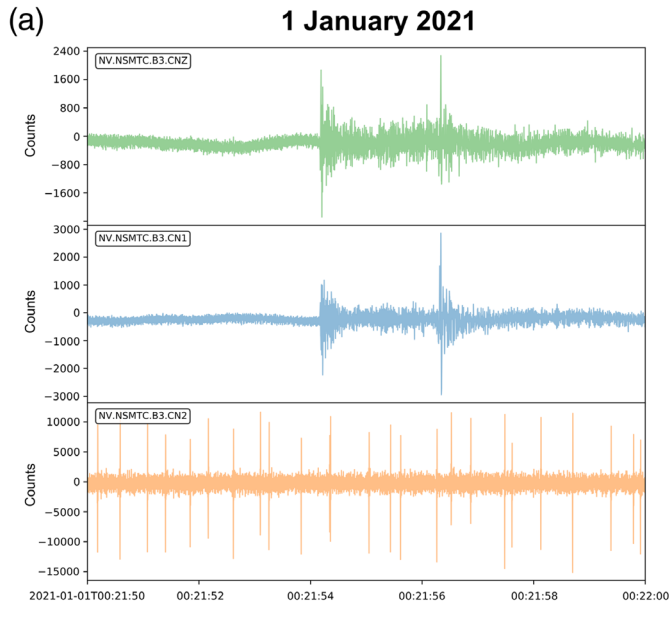
sensors are represented by location codes B1, B2, and B3 in order of increasing depth. The gain of the NSMTC Reftek dataloggers changed a number of times over the first four months of the deployment but has remained unchanged since 2 January 2018. The correct gain values at various points in time are reflected as distinct channels in the metadata available at the Incorporated Research Institutions for Seismology Data Management Center (IRIS DMC).

Besides the NSMTC sensors, there are a number of other seismic stations installed near the ONC headquarters. The

TABLE 2
Sensor Location Codes, Depths, and Sensor Types in the North Saanich Marine Technology Centre Borehole

Location Code	Depth (m)	Sensor
G1	0	Geospace HS-1-LT
B1	243.8	SA-ULN
B2	274.3	SA-ULN
В3	304.8	SA-ULN
G2	307.8	Geospace GS-11D

SA-ULN, Silicon Audio Ultra-Low Noise.



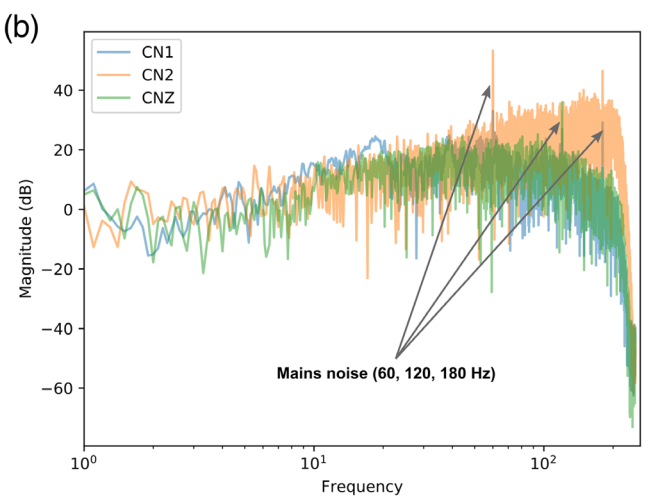


Figure 2. (a) Raw waveforms for a single, three-somponent Silicon Audio Ultra-Low Noise (SA-ULN) sensor (NV.NSMTC.B3) on 1 January 2021,including a local microearthquake visible on the vertical channel and channel CN1. Channel CN2 shows 3–4 electrical spikes per second and much higher noise, in general, above ~20 Hz. (b) Spectra for each channel showing the increased high-frequency noise for channel CN2 relative to CNZ and CN1, particularly mains electrical noise and its harmonics. Sensor B3 is the only sensor for which this issue is present. Sensors B1 and B2 are operating normally. The color version of this figure is available only in the electronic edition.

UNAVCO Plate Boundary Observatory (PBO) operates three boreholes within 500 m of the NSMTC borehole (PB.B009, PB.B010, and PB.B011). Each of these boreholes contains a large number of sensors, including geophones, strain meters, temperature sensors, and pore pressure sensors. Here,we use the data from the downhole geophone at station PB.B011 (depth 218 m; Geospace HS-1-LT), 175 m from NSMTC. In addition, the Canadian backbone seismic network (CN; Natural Resources

Canada [NRCAN Canada], 1975) operates station PGC roughly 450 mwest–northwest of the NSMTC wellhead (Fig. 1). This station consists of one Nanometrics Trillium 120 s posthole broadband sensor and one Nanometrics Titan 4g strong motion sensor. Here, we use the Trillium 120 posthole for the purposes of comparison to the SA-ULNs.

Data Quality and Availability

Data from the NV.NSMTC station are available from the IRIS DMC from 19 August 2017 until 19 March 2021. Following 19 March 2021, telemetry ceased, but cards are still being swapped and data will be uploaded to the IRIS DMC. Data from CN.PGC and PB.B011 are also available through the IRIS DMC.

To date, all the sensors are functioning normally, more than four years after installation. The single exception is channel NV.NSMTC.B3.CN2—a horizontal channel on the deepest Silicon Audio sensor, which exhibits much higher energy electrical noise than the other SA-ULN channels (specifically 60 Hz noise). Figure 2 shows sensor B3's waveforms and spectra surrounding a local earthquake on 1 January 2021. The spikes on CN2 are obvious in the time and frequency domain. This was noticed during installation and testing, and was determined to be related to the downhole instrumentation; but the exact cause is unknown. All other channels for NSMTC behave normally.

A final important note is that the vertical components of the ASIR-packaged Silicon Audio accelerometers are wired with positive acceleration down in a right-handed coordinate system. This is reported correctly in the metadata archived at IRIS using the "dip" attribute of the CNZ channel for each sensor. For the orientation analysis reported in the following, this was accounted for. Future users should take care to account for this when using these data, as the flipped polarity of the Z component with respect to the earthquake seismology standard will not be accounted for when using the response removal functionality of ObsPy (Krischer *et al.*, 2015), for example.

Borehole sensor orientation

When a sensor is installed in a deep borehole or on the ocean floor, the orientation of the horizontal components is typically unknown; though the vertical component is usually assumed to be vertical. Doran and Laske (2017) determined the in situ orientations of the horizontal components of ocean bottom instruments using the polarization of the Rayleigh-wave arrival waveform, which appears only on the vertical and radial components of a seismogram when rotated into a ray-based coordinates. They rotate the raw, three-component seismogram through all the possible orientations (assuming a vertical Z component) to find the maximum correlation between the radial component and the 90° phase-shifted vertical component (i.e., the Hilbert transform). The measurements are performed multiple times per earthquake using seven different bandpass filters to

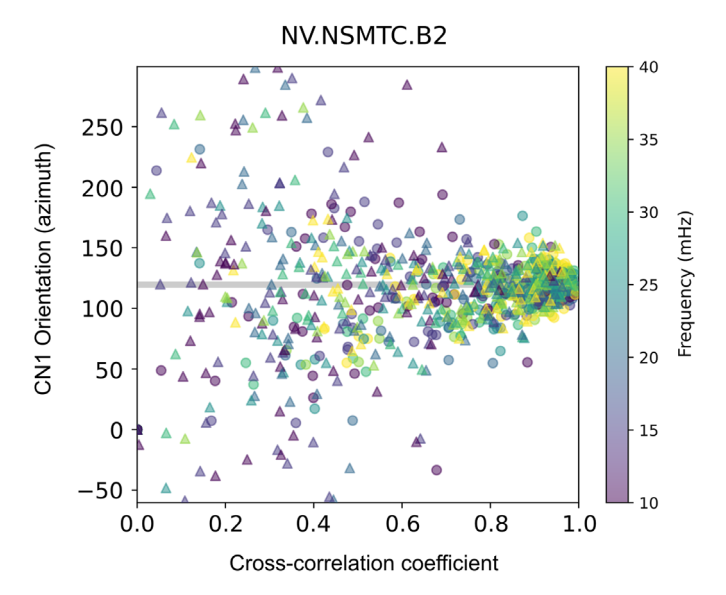


Figure 3. Orientation of the CN1 component of NV.NSMTC.B2 as a function of cross-correlation coefficient (between radial component and Hilbert transformed vertical component). Each measurement is colored by the central frequency of the bandpass filter that was applied to the waveforms being correlated. Triangles represent a measurement of the R_2 (major arc) Rayleigh arrival, whereas circles represent R_1 (minor arc) arrivals. Only measurements with a cross-correlation coefficient of >0.8 were accepted. The final orientation for the component is shown as a gray bar in the background with a width corresponding to the four-sigma error. The color version of this figure is available only in the electronic edition.

reduce biases related to laterally heterogeneous wave propagation (Doran and Laske, 2017). In addition, both the minor (the shortest distance, R_1) and the major (long way around, R_2) great circle Rayleigh paths are considered for each event. This further eliminates uncertainty due to the R_2 arrival often exhibiting a higher signal-to-noise ratio (SNR) than the R_1 due to R_1 's contamination by Love-wave coda and Rayleigh overtones (Doran and Laske, 2017). We performed the same analysis on each of the downhole instrument at NSMTC and report the results of this analysis in Table 3. We used all the events worldwide of $M_{\rm w} > 6.5$ for this analysis. A calculated azimuth was only accepted if the cross-correlation coefficient between the Hilbert-transformed vertical component and the rotated radial component exceeded 0.8. The number of accepted measurements per sensor is reported in the final column of Table 3. The azimuths in Table 3 indicate the orientation of the first horizontal component of the sensor (e.g., CN1), with the second component (e.g., CN2) oriented 90° clockwise from the first. Figure 3 shows the orientation angle of NV.NSMTC.B2.CN1 for each earthquake as a function of cross-correlation coefficient, colored by the central frequency of the passband for each measurement. Triangles indicate measurements of the R_2 path, whereas circles indicate the R_1 path.

TABLE 3
Results of the Orientation Analysis for Component CN1

Location Code	Mean Azimuth (°)	Error (°)	Number of Events Used
B1	232.31	2.68	52
B2	119.56	2.68	57
B3	252.60	7.11	32
G2	147.75	7.99	14

The mean azimuth is reported as the sensor azimuth in the sensor metadata archived at Incorporated Research Institutions for Seismology. Values are degrees clockwise from north.

Initial Observations

Figure 4 shows the amplitude and phase response curves for each of the sensors in Figure 1. The amplitude units in the top panel are velocity and in the second panel are acceleration. The SA-ULN's flat response is wider than for any other instrument with the exception of the Titan strong motion sensor, which is flat to 0 Hz. The high-frequency end of the SA-ULN's flat response is about one order of magnitude higher than a broadband sensor, whereas the low end of the flat response is at least two orders of magnitude lower than a typical geophone.

Noise spectra

Figure 5 shows the mean power spectral density (PSD) for selected sensors on the vertical component. Each PSD was calculated from one year (2018) of continuous waveforms using the methodology of McNamara and Buland (2004), as incorporated into the ObsPy library (Krischer et al., 2015). The Peterson (1993) high- and low-noise models are depicted in gray for comparison, with frequency increasing to the right. The region between the 10th- and 90th-percentile PSD is shaded surrounding the median for each curve. The modeled self-noise of the SA-ULN sensors is shown as a gray dot-dashed line. When comparing the SA-ULN (blue) to the other sensors, there are three broad trends. Moving from low frequency to high:

- 1. The SA-ULN has a noise floor just below the Peterson highnoise model for frequencies below 0.1 Hz (10 s). This is 10–40 dB better than for any of the other instruments, with the exception of the Trillium 120 posthole broadband at PGC. This illustrates an important point: the SA-ULN is not a replacement for a dedicated broadband instrument at frequencies <0.1 Hz, especially for applications focused on small-amplifude signals (e.g., inferring Earthstructure from $M_{\rm w}$ < 6 earthquakes at teleseismic distances).
- 2. All sensors have a similar noise floor within the passband of the oceanic microseisms. While not identical, the regions between the 10th and 90th perentiles overlap significantly

for all sensors. Because Sidney, British Columbia, is located on the Pacific coast, the energy in the oceanic microseism here is large and masks any potential differences in sensor performance.

3. Above approximately 1 Hz, the noise floors again diverge. Here, the SA-ULN exhibits the lowest noise floor of any instrument and increasingly so at frequencies >10 Hz. NSMTC was sampled at 500 Hz and the surrounding stations at 100 Hz, so the plots stop at a Nyquist frequency of 250 and 50 Hz, respectively. Were all stations sampled at a kilohertz or more, the discrepancy between the SA-ULN and all other instruments would likely be even more pronounced. However, as shown by the modeled self-noise curve, the sensor self-noise increases to meet the measured year-long PSD at ~100 Hz, indicating that the sensor's self-noise and not the characteristics of the installation might limit the ability to detect signals above ~100 Hz.

The comparison shown in Figure 5 should be treated as a first approximation of the differences between the sensors. The comparisons between the SA-ULN (blue), the geophone in the NSMTC borehole (red), and the geophone in the PBO borehole B011 (green) are fair, given their proximity and similar mode of installation. However, the rest of the instruments are installed at the sur-

face and are, therefore, subject to significantly higher noise than the borehole stations. It is, therefore, difficult to assess whether reductions in noise for the borehole stations are due

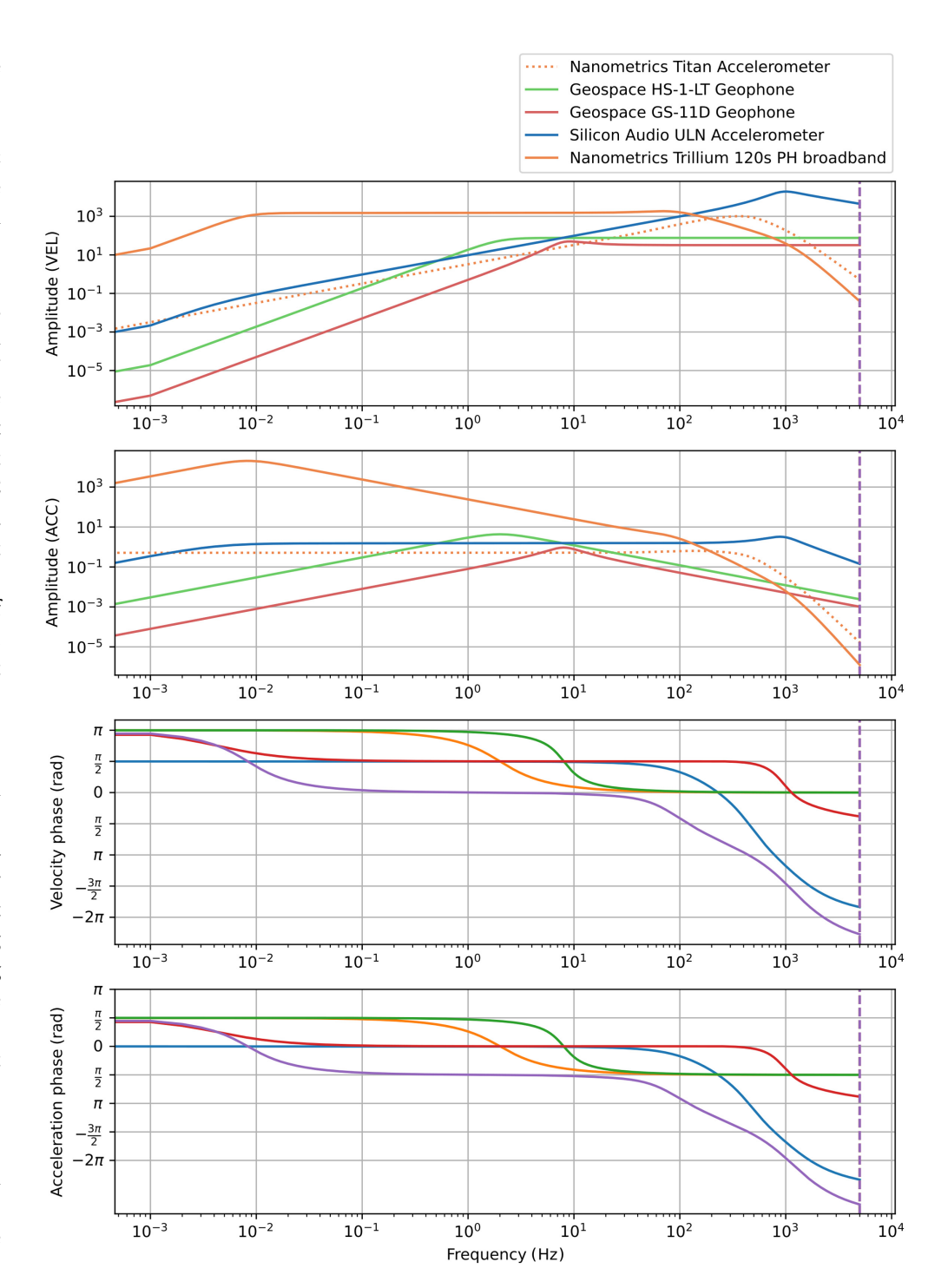


Figure 4. Bode plot for the instruments installed at site NSMTC or within 500 m and used in this analysis. Shown are the responses archived with thelncorporated Research Institutions for Seismology Library of Nominal Responses for Seismic Instruments for the vertical components of each instrument with the phase response unwrapped. Amplitudes are in units of velocity for the top panel and units of acceleration for the second panel. The color version of this figure is available only in the electronic edition.

to a low-noise environment or a low-noise sensor. Nevertheless, the data show a significant decrease in noise for the SA-ULN, when compared to the two borehole geophones.

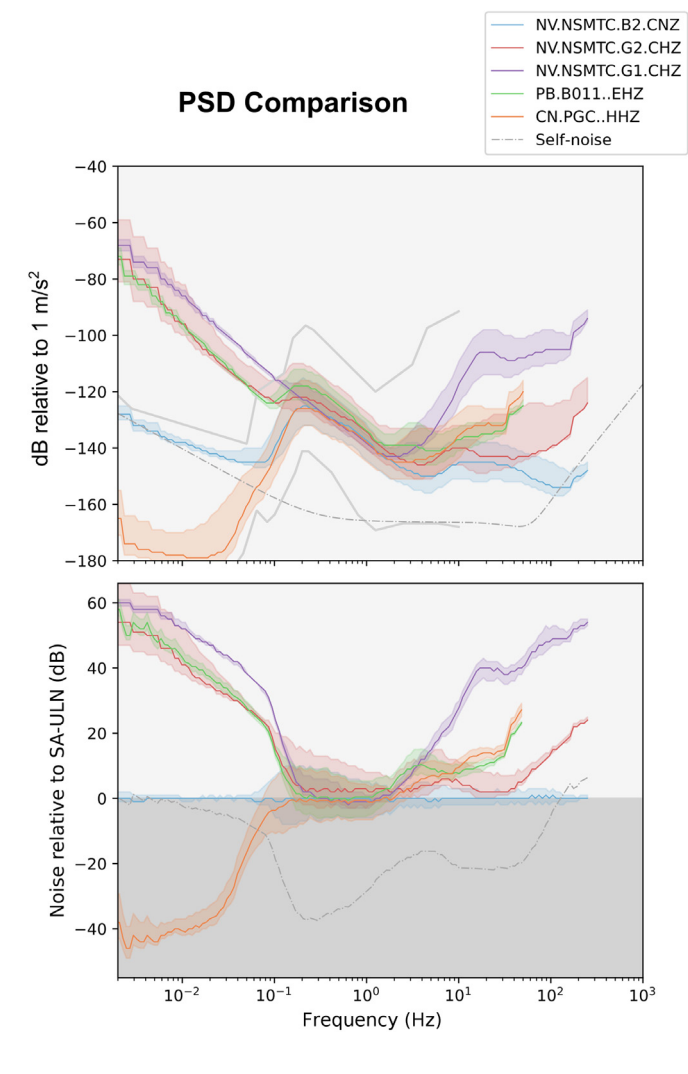


Figure 5. Median power spectral densities for the vertical component of the various sensor types at or near the NSMTC borehole. One Silicon Audio accelerometer is shown in blue. The *x* axis has units of frequency. The Peterson (1993) high- and lownoise models are shown in gray for reference. The bottom panel shows the difference between the Silicon Audio curve in the top panel and all other power spectral density (PSD) curves. Values below zero indicate a lower noise than the Silicon Audio for a given frequency. For both the panels, the color-filled area surrounding the curves represents the region between the 10th- and 90th-percentile PSD. The gray dot-dashed line shows the SA-ULN self-noise model. The color version of this figure is available only in the electronic edition.

Local microseismicity

Figure 6 shows two earthquakes recorded on four sensors: one $M_{\rm L}$ 1.33 at ~34 km and one $M_{\rm L}$ 4.6 at 135 km. Figure 6a,b shows two surface stations: CN.PGC.HHZ (broadband, orange) and NV.NSMTC.G1.CHZ (geophone, purple). Figure 6c,d shows the two sensors at the bottom of the borehole NV.NSMTC.B3.CNZ (SA-ULN, blue) and NV.NSMTC.G2.CNZ (geophone, red). The SNR is reported for each trace in the top right with a 7 s noise window and

15 s signal window. For this particular example, the borehole stations show higher SNR than the surface stations, given their low-noise location. There is a slight increase in the SNR for the Silicon Audio instrument relative to the downhole geophone (Fig. 6c,d). The apparent corner frequency of the events shown in Figure 6 is tens of hertz, a frequency at which the SA-ULN shows only an ~5 dB noise improvement relative to the downhole geophone (Fig. 5). Observe also the much larger amplitudes of the surface geophone at NSMTC (purple curves), particularly for S-wave arrivals. We suspect this is a site-related amplification effect. This instrument is direct buried on top of the man-made levee at the location of the wellhead in contrast to the PGC instrument, which is housed in a dedicated vault.

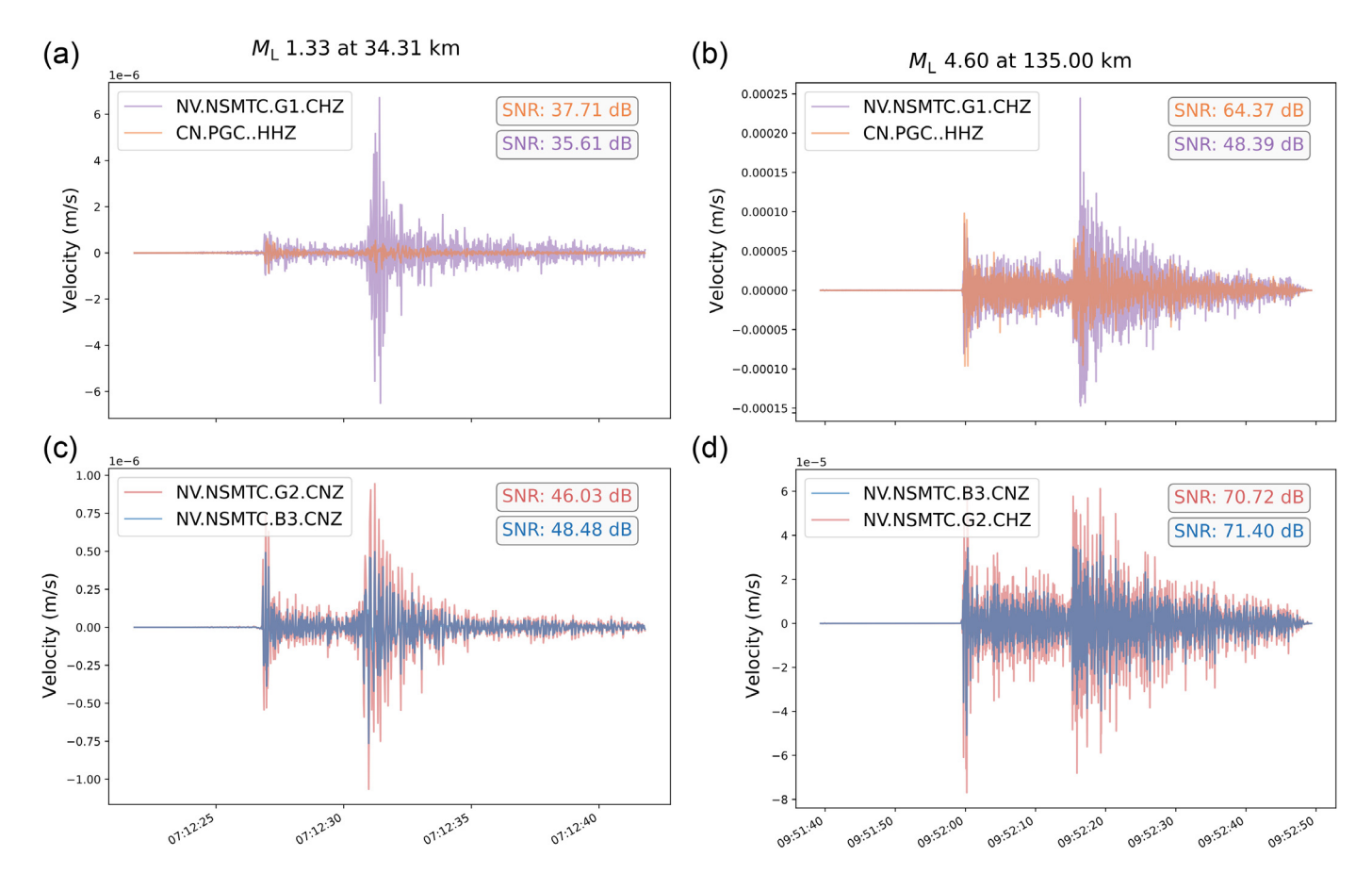
Detection thresholds

For smaller magnitude seismicity ($M_{\rm L}$ < 0) at event-station distances of less than 1 km, the sensors should record much higher frequencies (hundreds of hertz to kilohertz). The SA-ULN would be expected to more easily detect these signals, as its noise floor at 100+Hz is at least 20 dB less than the downhole geophone (red, Fig. 5). There are no located events in the U.S. Geological Survey Comprehensive Earthquake Catalog or Natural Resources Canada earthquake databases small enough or close enough to the NSMTC borehole to easily test such a scenario directly. However, Figure 7 shows simple modeling of the expected power spectra from small, nearby seismicity superimposed on the mean PSD calculations shown in Figure 5. We modeled the earthquake PSDs following the approach of Ackerley (2012). They use the simplification of the Brune (Brune, 1970) displacement spectrum of Abercrombie (1995):

$$\Omega(f) = \frac{\Omega_0}{(1 + (\frac{f}{f_c})^{\gamma n})^{\frac{1}{\gamma}}} e^{-\frac{nfr_h}{Q\sqrt{V_s V_r}}},\tag{1}$$

in which r_h is the source–receiver distance, y and n describe the "sharpness" of the high-frequency falloff rate, f_c is the event corner frequency, Ω_0 is the amplitude of the low-frequency plateau, Q is the quality factor, and V_s and V_r are the phase velocity at the source and receiver, respectively (we use S-wave velocities, as this is likely the highest SNR phase for local seismicity). Here, we use n=2 and y=2 following the findings of Abercrombie (1995) for small earthquakes. We take representative values for granite to approximate the setting of the NSMTC borehole with Q=200, $V_s=3500$ m/s, and $V_r=3200$ m/s. The slight difference in velocities at the source and receiver is meant to simulate a higher degree of weathering at the boreholes station, as it is closer to the surface. However, these values do not strongly affect the spectrum. We calculate Ω_0 following Aki and Richards (2002):

$$\Omega_0 = \frac{F_R S_a}{4\pi \sqrt{\rho_r \rho_s V_r V_s^5}} \frac{M_0}{r_h},\tag{2}$$



with $F_R=1$ for borehole sensors (a value of 2 would represent a surface installation) and $S_a=\frac{2}{\pi}$ describing the radiation pattern. We use 3.38 and 3.32 g/cm³ for ρ_s and ρ_r , respectively. To calculate the corner frequency, we assume a circular fault following Brune (1970):

$$f_c = \frac{2.36 \, V_s}{2\pi \, R_0},\tag{3}$$

and Eshelby (1957) who define the fault radius, R_0 , as,

$$R_0 = \sqrt[3]{\frac{7}{16} \frac{M_0}{\sigma_0}}. (4)$$

We assume a stress drop for each event of 3 MPa. Ackerley (2012) then computes the maximum amplitude of a wavelet as a function of frequency:

$$x_{\text{max}}(f) = 2|\Omega(f)|k_{\text{RBW}}f,\tag{5}$$

in which the relative bandwidth factor, $k_{\rm RBW}$, is $\frac{1}{\sqrt{2}}$ after the octave-width bandpass filters used in Clinton and Heaton (2002). Finally, the power spectra of the displacement spectrum described previously is (Ackerley, 2012),

$$P(f) = \left(\frac{x_{\text{max}}(f)}{k_{\text{crest}}}\right)^2 \frac{1}{k_{\text{RBW}}f},\tag{6}$$

Figure 6. Signal comparison for (a,c) a local microearthquake and (b,d) the largest regional event in the dataset recorded on the vertical channels at stations NSMTC and PGC. All waveforms are in units of velocity (m/s) and bandpass filtered between 2 and 20 Hz. Panels (a) and (b) compare the Trillium posthole broadband (orange) to the Geospace HS-1-LT geophone at the wellhead of the NSMTC borehole (purple). Panels (c) and (d) show the signal on one SA-ULN (blue) compared to the downhole Geospace GS11D geophone (red). The signal-to-noise ratio for each waveform is indicated in the upper right corner of each panel. The color version of this figure is available only in the electronic edition.

in which $k_{\rm RBW}f$ is the root mean square (rms) signal in a particular octave-width band, and $k_{\rm crest}$ converts the rms to a peak amplitude. We take $k_{\rm crest} = \sqrt{\frac{\pi}{2}}$ after Ackerley (2012).

Figure 7a shows the power spectra for theoretical $M_{\rm w}$ 0 and 1 events at 70 km from the sensors, similar to the event shown in Figure 6. At that magnitude and distance, our simple model suggests that a magnitude 1 event would barely meet or exceed the noise floor for the Silicon Audio instrument. Figure 7b shows the modeled power spectra for events at 1 km from the sensors. For this case, similar to what might be expected for monitoring of induced seismicity in a reservoir, the corner frequencies arehundreds of hertz. At these frequencies, Figure 7b qualitatively indicates that the SA-ULN could produce nearly a full magnitude unit decrease in the detection

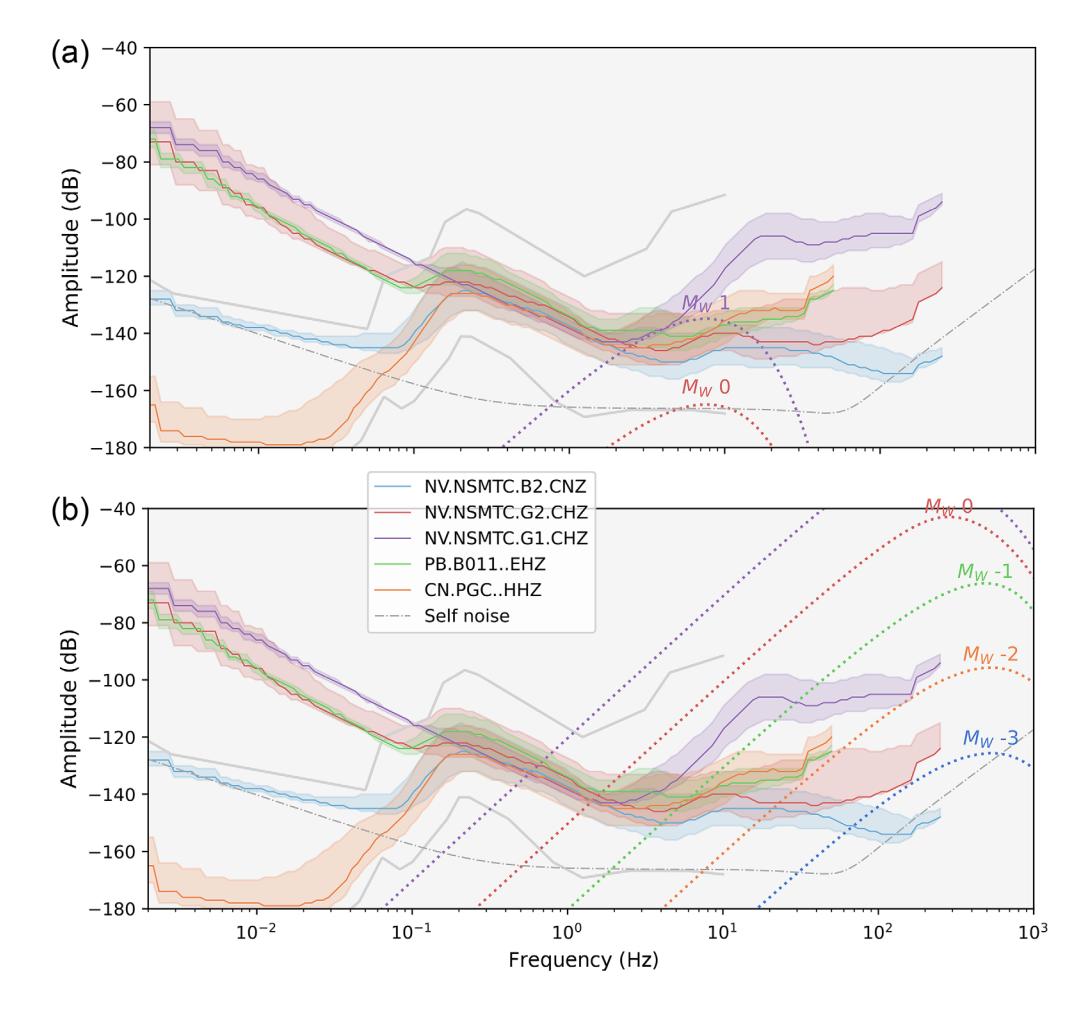


Figure 7. Year-long PSDs from Figure 5 overlain with modeled PSDs for various earthquakes assuming $V_s = 3500$ m/s, $V_r = 3200$ m/s, Q = 200, and a stress drop of 3 MPa.(a) Earthquake PSDs (dotted lines) for events at a distance of 70 km from the sensor. (b) PSDs for events at 1 km from the sensor The color version of this figure is available only in the electronic edition.

threshold relative to an industry-standard geophone. At frequencies exceeding 100 Hz, the SA-ULN detection threshold becomes defined by the sensor self-noise, which increases linearly with increasing frequency. For events at 1 km from the station, our models indicate that the sensor self-noise would limit the detection threshold of the SA-ULN to somewhere between $M_{\rm w}$ –3 and –4.

Summary

Here, we detailed a deep borehole drilled in Sidney, British Columbia, Canada, on Vancouver Island in collaboration with ONC in the summer of 2017. The borehole aimed to assess the performance of low-noise, optical accelerometers relative to standard instruments like geophones and broadband sensors. Ideally, these new instruments could be used to improve the resolution of seismic techniques like downward-looking vertical seismic profiles or to monitor small, induced seismic events during reservoir stimulation. In addition, the borehole site is located above the intensely studied Cascadia subduction zone, where

these low-noise instruments could further improve the understanding of subduction zone dynamics.

We presented a brief comparison of the response characteristics of these Silicon Audio accelerometers with various "standard" sensors, such as strong motion accelerometers, broadband velocity instruments, and industry-standard geophones. The Silicon Audio sensors combine a number of aspects of each of these existing technologies, with a high-sensitivity, low-noise floor, and a passband from hundreds of seconds to 1.5 kHz. Three sensors were grouted into the NSMTC borehole at depths approaching 300 m and have been functioning for over four years without incident. We also calculated the orientation of the horizontal components of the borehole sensors using Rayleigh-wave arrival waveforms.

Year-long PSDs computed for the sensors in or near the NSMTC borehole show that the Silicon Audio sensors have a lower noise floor than all other sensors at frequencies greater

than 1 Hz. This noise reduction relative to other instruments increases with frequency out to at least 20 dB at 250 Hz, in which sensor self-noise begins to define the signal detection threshold. We found all the sensors to perform comparably in the oceanic microseism frequency band due to the coastal setting of the borehole. At periods greater than 10 s, the SA-ULN significantly outperforms geophones but is shown to be inferior to a Trillium posthole, class "B" broadband for detecting small-amplitude signals. The SA-ULN noise floor at these longer periods is just inside the Peterson high-noise model (Peterson, 1993) but is 10-20 dB higher than the Trillium. Local and regional seismicity recorded on the SA-ULN sensors shows betterSNRs in the borehole relative to the surface, as expected. However, because the nearby sensors were only sampled at 100 Hz, we cannot directly observe the difference between the PDFs at higher than 50 Hz,in which the SA-ULNs are likely to exhibit significantly lower measured noise.

Finally, we modeled the Brune displacement spectrum for nearby, small-magnitude events and compared them to the power spectra of recorded noise to make a qualitative assessment of earthquake magnitude detection thresholds. For events at 1 km from the borehole, the SA-ULN would likely be able to detect events one magnitude unit smaller than those detected by a colocated geophone.

Data and Resources

All data detailed here are archived and publicly accessible through Incorporated Research Institutions for Seismology (IRIS). The NSMTC station metadata can be accessed at http://ds.iris.edu/mda/NV/NSMTC/?starttime=2017-08-18&endtime=2599-12-31.

CN.PGC and PB.B011 are also accessible through IRIS. Waveform retrieval was done using the International Federation of Digital Seismograph Networks (FDSN) client functionality in ObsPy (Krischer et al., 2015), as was the calculation of the power spectral densities (PSDs), plotting of instrument response curves, and retrieval of the Peterson noise models. Additional Silicon Audio data are available at the FORGE geothermal testbed (utahforge.com) under SEED id UU.FORK.01.?N? (University of Utah, 1962). The metadata are available at https://ds.iris.edu/mda/UU/FORK/?starttime=2019-04-10&endtime=2599-12-31. All the websites were last accessed on February 2022. Supplemental material for this article includes more detailed explanations of the gain correction process for PB.B011 and the process of estimating the orientation of the horizontal channels in NV.NSMTC. Also included is the catalog of events used in the DLOPy workflow.

Declaration of Competing Interests

The authors acknowledge that there are no conflicts of interest recorded.

References

- Abercrombie, R. E. (1995). Earthquake source scaling relationships from -1 to 5 ml using seismograms recorded at 2.5-km depth, *J. Geophys. Res.* **100**, no. B12, 24,015–24,036.
- Ackerley, N. (2012). Estimating the spectra of small events for the purpose of evaluating microseismic detection thresholds, *CSEG Geo-Convention*, Calgary, Alberta, Canada, 14–18 May 2012.
- Aki, K., and P. G. Richards (2002). *Quantitative Seismology*, University Science Books, Mill Valley, California.
- Benioff, H., F. Press, and S. Smith (1961). Excitation of the free oscillations of the Earth by earthquakes, *J. Geophys. Res.* **66**, no. 2, 605–619. Brune, J. N. (1970). Tectonic stress and the spectra of seismic shear waves from earthquakes, *J. Geophys. Res.* **75**, no. 26, 4997–5009.

- Clinton, J. F., and T. H. Heaton (2002). Potential advantages of a strong-motion velocity meter over a strong-motion accelerometer, *Seismol. Res. Lett.* **73**, no. 3, 332–342.
- Doran, A. K., and G. Laske (2017). Ocean-bottom seismometer instrument orientations via automated rayleigh-wave arrival-angle measurements, *Bull. Seismol. Soc. Am.* **107**, no. 2, 691–708.
- Eshelby, J. D. (1957). The determination of the elastic field of an ellipsoidal inclusion, and related problems, *Proc. R. Soc. Lond. Ser. A. Math. Phys. Sci.* **241**, no. 1226, 376–396.
- Krischer, L., T. Megies, R. Barsch, M. Beyreuther, T. Lecocq, C. Caudron, and J. Wassermann (2015). ObsPy: A bridge for seismology into the scientific python ecosystem, *Comput. Sci. Discov.* 8, no. 1, 014003.
- Marusiak, A. G., N. C. Schmerr, D. N. DellaGiustina, B. Avenson, S. H. Bailey, V. J. Bray, J. I. Brodbeck, C. G. Carr, P. H. Dahl, N. Habib, et al. (2021). The deployment of the seismometer to investigate ice and ocean structure (siios) in northwest Greenland: An analog experiment for icy ocean world seismic deployments, *Seismol. Soc. Am.* **92**, no. 3, 2036–2049.
- McNamara, D. E., and R. P. Buland (2004). Ambient noise levels in the continental United States. *Bull. Seismol. Soc. Am.* **94**, no. 4, 1517–1527.
- Natural Resources Canada (NRCAN Canada) (1975). Canadian National Seismograph Network, *International Federation of Digital Seismograph Networks*, available at https://www.fdsn.org/networks/detail/CN/ (last accessed February 2022).
- Ocean Networks Canada (2009). Neptune seismic stations, International Federation of Digital Seismograph Networks, available at https://www.fdsn.org/networks/detail/NV/ (last accessed February 2022).
- Peterson, J. R. (1993). Observations and modeling of seismic background noise, U.S. Geol. Surv. Open-File Rept. 93-322, doi: 10.3133/ofr93322.
- Plenkers, K., G. Kwiatek, M. Nakatani, and G. Dresen (2010). Observation of seismic events with frequencies f> 25 kHz at Mponeng deep gold mine, South Africa, *Seismol. Res. Lett.* **81,** no. 3, 467–479.
- University of Utah (1962). University of Utah regional seismic network, *International Federation of Digital Seismograph Networks*, available at https://www.fdsn.org/networks/detail/UU/ (last accessed February 2022).

Manuscript received 30 November 2021 Published online 11 April 2022